CONF-950740--54

UCRL-JC-120300
PREPRINT

Modeling the Dynamic Crush of Impact Mitigating Materials

R. W. Logan
L. D. McMichael

This paper was prepared for submittal to
ASME Pressure Vessel and Piping Division Conference
Honolulu, Hawaii
July 23–27, 1995

May 12, 1995

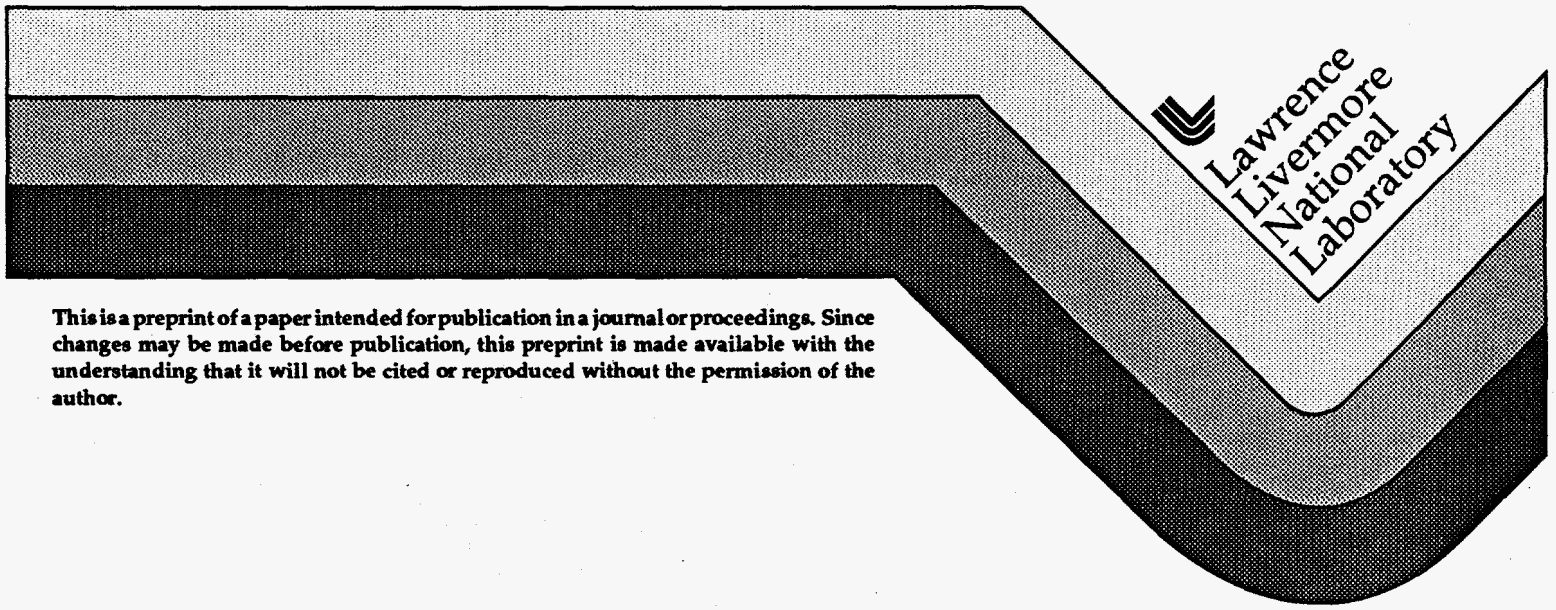

GH

MODELING THE DYNAMIC CRUSH OF IMPACT MITIGATING MATERIALS

Roger W. Logan
Larry D. McMichael
University of California
Lawrence Livermore National Laboratory
Livermore, California

ABSTRACT

Crushable materials are commonly utilized in the design of structural components to absorb energy and mitigate shock during the dynamic impact of a complex structure, such as an automobile chassis or drum-type shipping container. The development and application of several finite-element material models which have been developed at various times at LLNL for DYNA3D will be discussed. Between the models, they are able to account for several of the predominant mechanisms which typically influence the dynamic mechanical behavior of crushable materials. One issue we addressed was that no single existing model would account for the entire gambit of constitutive features which are important for crushable materials. Thus, we describe the implementation and use of an additional material model which attempts to provide a more comprehensive model of the mechanics of crushable material behavior. This model combines features of the pre-existing DYNA models and incorporates some new features as well in an invariant large-strain formulation. In addition to examining the behavior of a unit cell in uniaxial compression, two cases were chosen to evaluate the capabilities and accuracy of the various material models in DYNA. In the first case, a model for foam filled box beams was developed and compared to test data from a 4-point bend test. The model was subsequently used to study its effectiveness in energy absorption in an aluminum extrusion, spaceframe, vehicle chassis. The second case examined the response of the AT-400A shipping container and the performance of the overpack material during accident environments selected from 10CFR71 and IAEA regulations.

1. INTRODUCTION AND MOTIVATION

An important aspect of accurately predicting the response of a fissile material shipping container during impact is the ability to characterize the mechanical behavior of the impact mitigating material. Rigid cellular materials, such as rigid polyurethane, polyethylene, and polystyrene foams and fiberboard, are commonly used in shipping containers because of their ability to mitigate the impact generated shock loading transferred through the overpack and into the containment vessel. These materials have the potential to dissipate a large fraction of the impact kinetic energy through plastic volumetric deformation. In this paper, we will concentrate on the behavior of rigid foams, however, a wide range of commonly used impact mitigating materials, including honeycombs, share many of the same mechanical traits. There are numerous publications which discuss the mechanical behavior of rigid cellular materials in more detail, including Gibson and Ashby (1988), Maiti et al. (1984), and Green et al. (1969). The qualitative aspects of the mechanical behavior of rigid foams can be summarized as follows. The mechanical properties of rigid foams tend to be transverse isotropic, with the properties in the direction of foam rise differing from those perpendicular to the direction of foam rise. The degree of anisotropy in the foam tends to decrease with increasing density of the foam. High-density foams, $\rho \approx 320\ \mathrm{kg/m^3}$ or greater, tend to be only mildly anisotropic. In tension, the stress-strain behavior is nearly linear until a brittle fracture occurs. The compressive plastic behavior of rigid foams is characterized by volumetric compaction and the tendency that once yielding has occurred, further axial displacement of a foam sample will result in virtually no lateral displacements. This tendency continues until the foam is compacted to the density of its parent material. The compressive yield strength of rigid foams varies nonlinearly with density and can be influenced greatly by strain rate, with the tendency that higher density foams are less sensitive to small variations in strain rate.

The development and application of several finite-element material models which have been developed at various times at the Lawrence Livermore National Laboratory (LLNL) to model crushable materials will be discussed in this work. For a number of years, several of these material models have existed in LLNL's

DYNA3D (Whirley and Hallquist, 1991) code for three-dimensional, nonlinear, dynamic analysis of solid and structural finite-element problems. To various degrees, these models are able to account for several of the predominant mechanisms which typically influence the dynamic mechanical behavior of crushable materials, including: volumetric crush, strain rate dependent yield strength, and strain dependent plastic flow stress. These models have fundamentally different approaches toward representing the mechanics of crushable material behavior. In some cases, the models use tabular user-defined curves to specify the governing relationships. In other cases, constitutive equations with user-defined parameters are used. One issue we addressed was that no single existing model would account for the entire gambit of important constitutive features for crushable materials. Thus, we describe the implementation and use of an additional material model into our internal prototype version, W-DYNA. This model attempts to provide a more comprehensive constitutive model by combining features of the pre-existing DYNA3D models, as well as adding some new features in an invariant large-strain formulation. The essence of the crushable material behavior we desire to capture with the constitutive model is shown in Fig. 1, which is a series of views depicting a constant crosshead speed uniaxial compression test. In the left-hand column of Fig. 1, a side view of the test is depicted at various stages of crush, while the right-hand column shows a plan or top view of the crush sequence. Typically, the material may crush to an axial true strain of magnitude $|\varepsilon| \geq 0.6$ or more, with little or no lateral strains associated. In this mode, commonly observed plastic anisotropy is not related to lateral strains but to the uniaxial stress required for crush. On full compaction, plastic flow commonly takes on the character of the parent material. This behavior may or may not be anisotropic, but in the case of compacted metals in particular we must account for the possibility. As full compaction or lock-up is reached, incompressible plastic flow results in lateral strains on further axial crush. If the fully compressed material exhibits plastic anisotropy, as is the case illustrated in Fig. 1, these lateral strains will be unequal, as seen in the plan view of the late stages of this compression test.

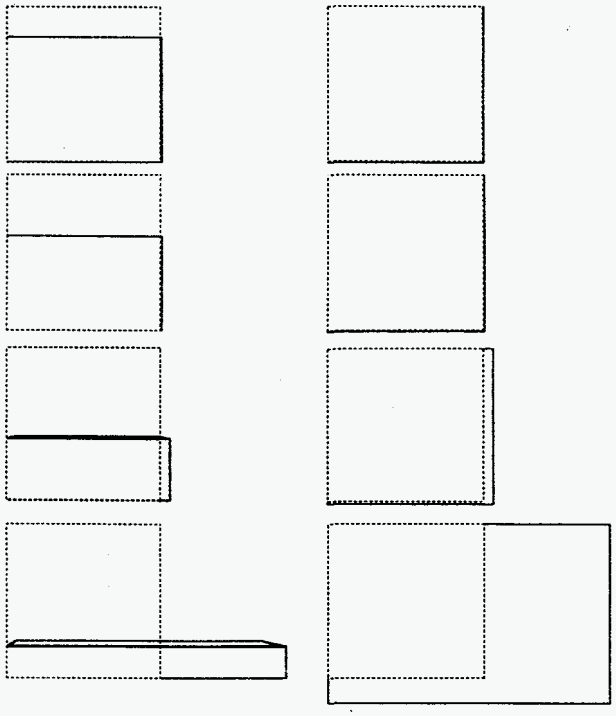

FIGURE 1. Graphical depiction of the stages of a uniaxial compression test using W-DYNA's Material Model 335 for anisotropic crush and deviatoric plasticity. The left-hand column is a side view, while the right-hand column is a plan or top view. Proceeding down each column, the engineering strain increment is 20% for each picture of the undeformed (dotted) and deformed (solid) element.

At LLNL, one aspect of our core missions is the evaluation of the effectiveness of shipping container overpack designs for impact protection of a nuclear component payload. For this purpose, DYNA analysis can be used either prior to physical testing, to determine the drop orientations most likely to induce maximum damage to the container, or after physical testing has been completed, to examine untested drop orientations. Once a reliable DYNA model is built, it can be used to predict the response of the container beyond the regulatory requirements to estimate a system factor of safety. Two cases were chosen to evaluate the capabilities and accuracy of the various material models in DYNA. In the first case, a model for foam filled box beams was developed and compared to test data from a 4-point bend test. The model was subsequently used to study the effectiveness of foam fill for energy absorption in an aluminum extrusion, spaceframe, vehicle chassis. We have found studies of spaceframe vehicle structures to be a highly leveraged dual-use activity for our skills in the evaluation of shipping containers, as the same design engineer can hone his or her skills by studying both problems. As an example of this leveraging, the second case examines the response of the AT-400A shipping container during accident environments selected from Title 10, Part 71 of the Code of Federal Regulations (10CFR71) and International Atomic Energy Agency (IAEA) Safety Series 6 (9 m drop of the container, and 9 m drop of a 500 kg plate onto the container respectively). The AT-400A is a drum-type container being developed for the shipment and storage of fissile material. The container uses high-density, rigid, polyurethane foam in the overpack for impact mitigation.

2. CONSTITUTIVE MODELS

Various constitutive models are available in the current version of DYNA3D that may be used to represent crushable materials. They each contain some of the features needed to represent the anisotropic crush and plastic flow of rate-dependent materials. However, as summarized in Table 1, none of the existing models contained all the features we anticipate needing for this and forthcoming studies of crush and compaction. Therefore, the final model in Table 1, Model 335, was incorporated into the W-DYNA version, and designated as such since it is in many ways a combination of the current Model 33 (Orthotropic Elastic-Plastic) and Model 35 (Augmented Forming Limit) in DYNA3D. Model 335 has the capability to model the anisotropic compaction region using two options: an invariant methodology abbreviated as HGDP, after Hill (1848), Gibson et al. (1989), and Drucker and Prager (1952), and a non-invariant methodology similar to Model 26, abbreviated as HHC (Hill plus Honey-Comb).

We proceed now to show briefly the interrelationship of explicit finite-element analysis formulation and the material constitutive equation. For the isotropic case, this (usually) culminates in the expression of effective stress using the von Mises isotropic expression. For a continuum, the equations of motion may be written:

$$\nabla \cdot \sigma + \rho \boldsymbol{b} = \rho \ddot{\boldsymbol{u}} \tag{1}$$

where σ is the Cauchy stress, $\boldsymbol{b}$ is the body force density field, ρ denotes the current material mass density, $\boldsymbol{u}$ is the displacement field, and a superimposed dot denotes differentiation with respect to time. Applying the finite element method to spatially discretize Eq. (1) yields a coupled set of nonlinear ordinary differential equations (ODEs) in time:

$$\boldsymbol{M}\ddot{\boldsymbol{u}} = \boldsymbol{f}^{ext}(t) - \boldsymbol{f}^{int}(\boldsymbol{u},t) \tag{2}$$

where $\boldsymbol{M}$ is a mass matrix, $\boldsymbol{u}$ is now a vector of nodal displacements, $\boldsymbol{f}^{ext}$ is a vector of externally applied time-dependent nodal forces, $\boldsymbol{f}^{int}$ is a vector of internal nodal forces arising from stresses existing in the elements, and t is time. Even if higher-order differential operators are included, such as those arising in beam, plate, and shell formulations, the resulting set of ODEs still retains the form of Eq. (2).

Next, the assumptions of explicit analysis are introduced to numerically integrate these ODEs in time. DYNA integrates Eq. (2) using the central difference method. To begin, assume that all quantities are known at time $t=t_n$ and it is desired to advance the solution to time $t=t_{n+1}$. The first step is to find the acceleration $\boldsymbol{a}_n \equiv \ddot{\boldsymbol{u}}(t_n)$ from the discrete version of Eq. (2) at time $t=t_n$:

$$\boldsymbol{M}\boldsymbol{a}_n = \boldsymbol{f}_n^{ext} - \boldsymbol{f}_n^{int} \tag{3}$$

where $\boldsymbol{f}_n \equiv \boldsymbol{f}(t_n)$. We now introduce a nodal lumped mass approximation, so $\boldsymbol{M}$ becomes a diagonal matrix, and the evaluation of $\boldsymbol{a}_n$ from Eq. (3) is very inexpensive since the equations are now uncoupled and all quantities on the right-hand side are known. The central difference method gives update equations for the nodal velocities $\boldsymbol{v}$ and displacements $\boldsymbol{u}$ as:

$$\boldsymbol{v}_{n+\frac{1}{2}} = \boldsymbol{v}_{n-\frac{1}{2}} + \boldsymbol{a}_n \Delta t \tag{4}$$

$$\boldsymbol{u}_{n+1} = \boldsymbol{u}_n + \boldsymbol{v}_{n+\frac{1}{2}} \Delta t \tag{5}$$

TABLE 1. Capabilities of Existing and New Material Models for Crush / Compaction in DYNA. Y="Yes" and N="No" for each feature indicated including coordinate invariance of the stress, Strain, Rate, and Pressure dependent yield, nonlinear pressure/volume crush behavior, and anisotropy of crush and compacted states.

Model No.	Description	Invariant	Yield (Strain)	Yield (Rate)	Yield (Press.)	Pressure /Volume	Aniso. Crush	Aniso. Deviator	TOTAL "N"'s
5	Soil & Crushable Foam	Y	N	N	Y	Y	N	N	4
10	Iso-Elastoplastic Hydro	Y	Y	N	Y	Y	N	N	3
16	Rebar/Concrete/Geologic	Y	Y	Y	Y	Y	N	N	2
25	Extended 2-Invar. Cap	Y	N	N	Y	Y	N	N	4
26	Metallic Honeycomb	N	N	N	N	Y	Y	N	5
37	3-Invariant Cap	Y	N	Y	Y	Y	N	N	3
335	HGDP* or HHC**	Y	Y	Y	Y	Y	Y	Y	0

* HGDP = Hill, Gibson, Drucker, Prager (invariant)

** HHC = Hill, Honey-Comb (non-invariant)

Now that the updated kinematic variables are known, the next step is to evaluate the forces on the right-hand-side of Eq. (3) at time $t=t_{n+1}$. Since external loads are usually prescribed functions of time, the evaluation of f_{n+1}^{ext} is straightforward. The bulk of the computations within a time step are expended to evaluate the internal force f_{n+1}^{int}. Computation of f_{n+1}^{int} begins with the calculation of the rate of deformation $d_{n+\frac{1}{2}}$ from:

$$d_{n+\frac{1}{2}} = \frac{1}{2}\left[\nabla v_{n+\frac{1}{2}} + \left(\nabla v_{n+\frac{1}{2}}\right)^{T}\right] = B v_{n+\frac{1}{2}} \tag{6}$$

where ∇v denotes the gradient of the velocity with respect to the geometry at time $t=t_{n+\frac{1}{2}}$, and B is the "strain-velocity operator." Next, the updated Cauchy stress σ_{n+1} is found from:

$$\sigma_{n+1} = \sigma_n + \int_{t_n}^{t_{n+1}} \dot{\sigma} dt \tag{7}$$

where $\dot{\sigma}$ is computed from an objective stress response function using the rate of deformation $d_{n+\frac{1}{2}}$ and material history variables. This incremental formulation easily accommodates material nonlinearities such as elastoplasticity and viscoplasticity. Finally the new internal force vector for an element e is found from the updated stresses using:

$$f_{n+1}^{int,e} = \int_{\Omega_e} B^T \sigma_{n+1} d\Omega_e \tag{8}$$

and the global force vector f_{n+1}^{int} is found by assembling contributions from all elements. This completes the update of all quantities from time $t=t_n$ to time $t=t_{n+1}$.

During this process, the effective stress, both trial and updated, is calculated (for the isotropic models) from the von Mises equation:

$$\bar{\sigma}^2 = \frac{(\sigma_2-\sigma_3)^2 + (\sigma_3-\sigma_1)^2 + (\sigma_1-\sigma_2)^2}{2} \tag{9}$$

For isotropic elastoplasticity, the stress update is performed using the radial return method. At this point, we illustrate the unique characteristics of the models chosen for this work as shown in Table 1 above.

2.1 Model 5: Soil and Crushable Foam

This model is perhaps the oldest implementation in DYNA3D of a crushable material model, with its origins due to Krieg (1972) and Key (1974). In this model, the deviatoric yield at any pressure p is given by:

$$\sigma_Y = \left[3(\mathbf{a}_0 + \mathbf{a}_1 p + \mathbf{a}_2 p^2)\right]^{\frac{1}{2}} \tag{10}$$

where the pressure p is related to the volumetric strain ε_v in a nonlinear input table (equation of state):

$$p = p(\varepsilon_v) \tag{11}$$

If we let $\mathbf{a}_1$=0, $\mathbf{a}_2$=3, and $\mathbf{a}_0$ equal a small positive 'seed' value, it is possible to use the non-associated flow Model 5 to approximate the stress-strain behavior in uniaxial crush, with minor lateral expansion during the crush phase. The positive 'seed' value is necessary to inhibit the tendency of the model to behave in a perfectly plastic manner. The material constitutive behavior is quite restricted since no allowance is made for anisotropy, deviatoric strain hardening, strain rate effects, or deviatoric behavior of the parent material.

2.2 Model 10: Isotropic Elasto-Plastic Hydrodynamic

Although not its primary intended application, this model can indeed be used to model crushable behavior with some advantages over Model 5 above. There are two options available in this material model to define the deviatoric yield σ_Y. For the first option, the deviatoric yield is related to the effective plastic strain $\bar{\varepsilon}^p$ in a nonlinear input table:

$$\sigma_Y = \sigma_Y(\bar{\varepsilon}^p) \tag{12}$$

For the second option, the deviatoric yield at any pressure p and effective plastic strain $\bar{\varepsilon}^p$ is given by:

$$\sigma_Y = \sigma_0 + E_p \bar{\varepsilon}^p + (\mathbf{a}_1 + \mathbf{a}_2 p)p \tag{13}$$

where σ_0 is the initial yield stress, E_p is the plastic modulus, p is the pressure, and $\mathbf{a}_1$ and $\mathbf{a}_2$ are user-defined constants. Both options require the pressure p to be related to the volumetric strain ε_v in a nonlinear input table as in Eq. (11). The first option allows the user to specify a general effective plastic strain dependent plastic flow stress, which can be used to simulate both the plateau stress and densification regions. The second option requires the user to determine a 'best fit' yield condition using the initial yield stress σ_0, plastic modulus E_p, and pressure hardening coefficients $\mathbf{a}_1$ and $\mathbf{a}_2$ (e.g. let $\mathbf{a}_1$=3, $\mathbf{a}_2$=0, and σ_0 again equal to a small positive 'seed' value). For this paper, we used the first option for the yield condition in order to specify a general stress-strain behavior which, when coupled with the defined

pressure-volumetric strain relationship, was able to approximate the stress-strain behavior in uniaxial crush, again with minor lateral expansion during the crush phase. Still, no allowance is made for anisotropy, strain rate effects, or deviatoric behavior of the parent material.

2.3 Model 16: Concrete / Geological Material

This model has its origins in an attempt to model reinforced concrete in a homogeneous fashion, and has in addition some of the greatest versatility in representing geologic materials. Once again, however, we must immediately constrain the non-associative yield condition:

$$\sigma_Y = \mathbf{a}_0 + \frac{p}{\mathbf{a}_1 + \mathbf{a}_2 p} \tag{14}$$

with values $\mathbf{a}_2$=0, $\mathbf{a}_1$=1/3, and $\mathbf{a}_0$ again equal to a small positive 'seed' value. Using these values, we can approximate true uniaxial response in a uniaxial compression test. Tabular strain hardening using $\bar{\varepsilon}^p$ is available, as is a tabular definition of strain-rate dependent deviatoric yield. However, use of either of these may upset the constrained relationship between yield and pressure which is necessary to inhibit large lateral strains in uniaxial compression. The pressure p is again related to the volumetric strain ε_v in a nonlinear input table as in Eq. (11).

2.4 Model 26: Metallic Honeycomb

Of the existing DYNA3D models, Model 26 is clearly the most suited for capturing uniaxial crush, especially under orthotropic conditions. During compaction in any of the three principal material directions *a*, *b*, and *c*, the stress is a function of relative volume V_r:

$$\begin{aligned} \sigma_a &= \sigma_a(V_r) \\ \sigma_b &= \sigma_b(V_r) \\ \sigma_c &= \sigma_c(V_r) \end{aligned} \tag{15}$$

with no plastic strain except in the direction of the associated stress in the material coordinate system. Similar (essentially uncoupled) terms are given for the shear stresses τ_{ab}, τ_{bc}, and τ_{ca}. In fact, the crush behavior of Model 26 may be viewed in terms of a continuum yield surface of the form:

$$\begin{aligned} \bar{\sigma}^m = &\left(\frac{\sigma_a}{D_a}\right)^m + \left(\frac{\sigma_b}{D_b}\right)^m + \left(\frac{\sigma_c}{D_c}\right)^m \\ &+ \left(\frac{\tau_{ab}}{D_{ab}}\right)^m + \left(\frac{\tau_{bc}}{D_{bc}}\right)^m + \left(\frac{\tau_{ca}}{D_{ca}}\right)^m \end{aligned} \tag{16}$$

where $m=\infty$, $\bar{\sigma}=\bar{\sigma}(V_r)$, and $D_{ab} = D_{bc} = D_{ca}$ as an imposed restriction in Model 26. Although we might envision this to be an invariant isotropic model for crush under conditions of isotropy, the result is not so. The model suffers from the limitations of its coordinate-system dependency, which may introduce errors in the magnitude of the stresses as high as a factor of $\sqrt{4/3}$ for off-axis loading. In addition, deviatoric strain and rate effects are unavailable, and the fully compacted material is limited to perfectly plastic von Mises behavior. Despite these limitations, Model 26 is the best pre-existing candidate for modeling uniaxial crush, especially in the anisotropic case.

2.5 Models 25 and 37: Cap Models

The two-invariant cap Model 25, in its compaction region, can be viewed to relate the von Mises effective stress to the first stress invariant ($3p$) with a constant defining the magnitude of the stress tensor at yield. If we take the pressure-hardening variable κ=0 for a moment, then:

$$X^2 = \left[\frac{\mathbf{R}^2 s_{ij} s_{ij}}{2} + (\sigma_x + \sigma_y + \sigma_z)^2\right] \tag{17}$$

Under conditions of uniaxial compression, we can certainly choose $\mathbf{R}$ to provide uniaxial crush with no lateral strains, given that this formulation uses associated flow. Further, Eq. (17) is invariant to the coordinate system chosen, unlike Eq. (16) for the honeycomb model. However, the restrictions of rate-independent flow and isotropy remain. The 3-invariant cap Model 37 can be set up in a similar manner, and although the rate-independent restriction is removed, the restriction to isotropy remains. Thus, rather than explore the use of these cap models in detail, we chose to extend them to the anisotropic case, using the features of two existing DYNA3D models to develop a new model to handle the general case for orthotropic compaction and subsequent orthotropic flow in the fully compacted state.

2.6 Model 335: HGDP and HHC Options

In the current DYNA3D, Model 33 (Orthotropic Elastic-Plastic) uses a quadratic yield function (Hill, 1948) given by:

$$\bar{\sigma}^2 = \frac{F(\sigma_b - \sigma_c)^2 + G(\sigma_c - \sigma_a)^2 + H(\sigma_a - \sigma_b)^2 + S}{R+1} \tag{18a}$$

Eq. (18a) relates the effective stress to the three normal components of Cauchy stress, with the term S containing the shear stress terms:

$$S = 2L\sigma_{bc}^2 + 2M\sigma_{ca}^2 + 2N\sigma_{ab}^2 \tag{18b}$$

The values for the constants in Eq. (18) can be expressed in terms of the strain ratios R, Q, and P as described in the DYNA3D manual and elsewhere, with the following additional relations needed:

$$F = R / P \tag{19a}$$
$$G = 1 \tag{19b}$$
$$H = R \tag{19c}$$

$$L = (Q_{bc} + \tfrac{1}{2})(R + 1) \tag{19d}$$
$$M = (Q_{ca} + \tfrac{1}{2})(R + Z) \tag{19e}$$
$$N = (Q_{ab} + \tfrac{1}{2})(1 + Z) \tag{19f}$$

This yield surface will certainly account for plastic anisotropy (and elastic anisotropy if an orthotropic elastic relation is used) for incompressible plastic flow, but makes no allowance for crush or compaction. The allowance for crush is accomplished in one of two ways. In each, the first step is to transform the stresses so that:

$$\begin{aligned} \sigma'_a &= (\sigma_a - \kappa)/X \\ \sigma'_b &= (\sigma_b - \kappa)/Y \\ \sigma'_c &= (\sigma_c - \kappa)/Z \\ \sigma'_{ab} &= (\sigma_{ab})/T \\ \sigma'_{bc} &= (\sigma_{bc})/T \\ \sigma'_{ca} &= (\sigma_{ca})/T \end{aligned} \tag{20}$$

where κ denotes the cap pressure as in Model 25, **X**, **Y**, **Z**, and **T** are functions of both the volumetric strain and a weighted deviatoric and volumetric strain rate:

$$\dot{\varepsilon}^* = \sqrt{d\bar{\varepsilon}^2 + d\varepsilon_v^2} / \Delta t \tag{21}$$

Then, in the cap or plastic crush region, we again express the yield surface as:

$$\bar{\sigma}^2 = \frac{F(\sigma'_b - \sigma'_c)^2 + G(\sigma'_c - \sigma'_a)^2 + H(\sigma'_a - \sigma'_b)^2 + S + C}{R + 1} \tag{22a}$$

where again the term S contains the normalized shear stress terms:

$$S = 2L(\sigma'_{bc})^2 + 2M(\sigma'_{ca})^2 + 2N(\sigma'_{ab})^2 \tag{22b}$$

and the cap term C takes one of two forms, either:

$$C_1 = A\left[\ (\sigma'_a) + (\sigma'_b) + (\sigma'_c)\ \right]^2 \tag{22c}$$

for the HGDP model, or:

$$C_2 = A\left[\ (\sigma'_a)^2 + (\sigma'_b)^2 + (\sigma'_c)^2\right] \tag{22d}$$

for the HHC model. Note that the HHC term suffers from the same restrictions as the yield function for Model 26 above due to lack of invariance. However, the C_2 term does allow, for A>>0, a clearer distinction between pure uniaxial crush and the incompressible flow of the compacted material. In general, however, the HGDP term C_1 is used in the remainder of this work. In both cases, the parameter A is a function of both position along the pressure p axis, and also a function of the degree of compaction. In the fully compacted state, A is set to A=0 thus assuring plastic flow of the compacted material under the 1948 Hill criterion. When $p < \kappa$, an approximation to the Drucker-Prager yield surface is used along with a tension cutoff for some specified value of $p < 0$. The stress update for Model 335 in the plasticity state proceeds with a calculation of the contact stresses σ_i^c and updated stresses σ_i^N from the previous stresses σ_i^n :

$$\sigma_i^c = \sigma_i^n + C_{ij}^e d\varepsilon_j^e \tag{23}$$
$$\sigma_i^N = \sigma_i^c + C_{ij}^{ep}(d\varepsilon_j - d\varepsilon_j^e) \tag{24}$$

Here, $d\varepsilon_j^e$ are the elastic portions of the strain increment, and C_{ij}^e is the elastic constitutive matrix. To obtain the updated stresses, we apply the remainder of the strain increment $(d\varepsilon_j - d\varepsilon_j^e)$ using the elastoplastic matrix C_{ij}^{ep} :

$$C_{ij}^{ep} = C_{ij}^e - \frac{C_{ij}^e q_j (C_{ij}^e q_j)^T}{p_i q_i + q_i^T C_{ij}^e q_j} \tag{25}$$

The yield surface $\mathcal{F}$ directly affects the calculation of the matrix C_{ij}^{ep}, since

$$q_i = \frac{d\mathcal{F}}{d\sigma_i} \tag{26}$$

$$p_i = -\frac{d\mathcal{F}}{d\varepsilon_i} \tag{27}$$

In addition to the anisotropy of crush and incompressible plasticity, the Model 335 constitutive behavior draws from DYNA3D's Model 35 (Forming Limit Diagram), in that the yield stress may be multiplied by a strain rate dependent factor found from load curve *LCEDM*. The first column of this load curve

should contain total strain rate values, and the second column should give the scale factor to be multiplied times the current yield stress, σ_Y. Note that this strain rate scaling is applied after strain hardening is taken into account, and applies to crush as well as deviatoric plastic flow. Although strain rate effects are not dominant for the high-density foams studied in this work, they are in fact quite significant for lower density, open and closed cell foams, thus, inclusion of this feature was felt to be essential. Next, we will demonstrate the effect of the chosen yield surface (Model 5, 10, 16, 26, or 335) on the material behavior calculated by DYNA for a uniaxial compression test

2.7 Behavior of the Material Models in a Simple Test

To examine the ability of the candidate DYNA Material Models to capture numerically the typical crush behavior of the rigid foams in question, a simple one-element cube was constructed and compressed at constant velocity with frictionless end conditions. This test was carried out with our best effort at generating a material data deck to represent the rigid, closed-cell, 480 kg/m^3 polyurethane foam to be used in the AT-400A application discussed later. Data decks were constructed for Model 5 (for both elastic-perfectly plastic behavior, and with an offset $\mathbf{a}_0 > 0$, $\mathbf{a}_1 = 0$, $\mathbf{a}_2 = 3$), Model 10, Model 16, Model 26, and Model 335. The calculated stresses were compared (Fig. 2a) against measured data from a uniaxial compression test. For Models 26 and 335, this is essentially an exercise in proper input of the data. For Models 5, 10, and 16, more care is required because of the $\sigma_Y = 3p$ relation that must be approximated. Even though there are non-unique data decks that would give the proper stress-strain curve, it is necessary in addition to attempt to approximate the uniaxial crush condition without producing lateral plastic strain. For Model 26, this condition is achieved automatically. For Model 335, it is achieved if the value A=1 is used for an isotropic material as used in this case. For Models 5, 10, and 16, the (somewhat successful) attempts to reproduce the stress-strain curve lead to various degrees of lateral motion as seen in the chart of lateral vs. axial displacement in Fig. 2b. An ideal lateral-to-axial displacement ratio is 0.0, while the actual ratios range from nearly 0 to ~0.7 for a maximum axial displacement of 0.50 in the unit cell. The best performers appear to be Model 26 and Model 335 (with their additional advantages of anisotropy for both and invariant isotropy for Model 335), with Model 5 "offset" and Model 10 as fairly good alternates.

3. APPLICATIONS - FOAM FILL OF BOX BEAMS

Foam-filling of hollow structural members has been proposed as a means to enhance the energy absorbing characteristics of spacefames intended for applications requiring crashworthiness. Foam may serve to increase the energy absorbed by a given member or to redirect energy absorption to other members by stiffening a given member.

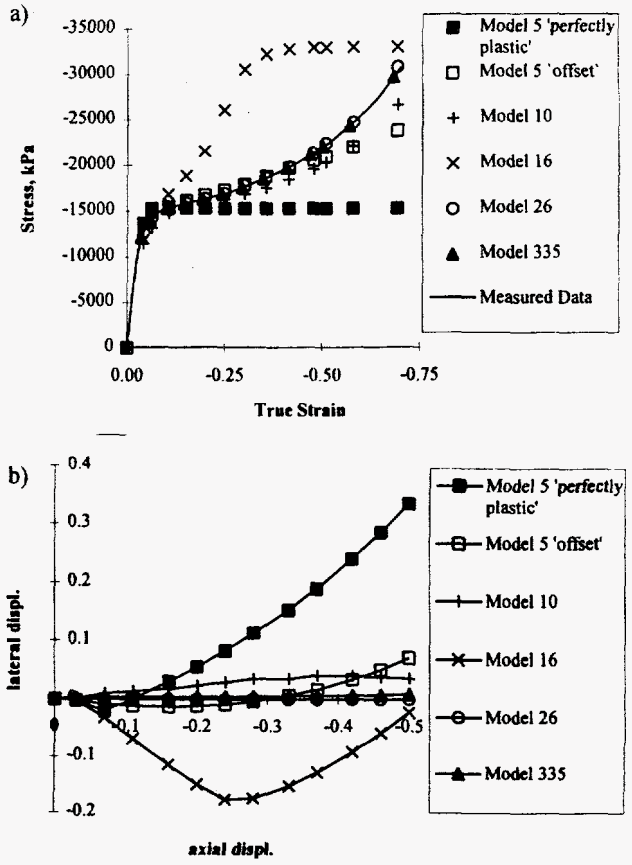

FIGURE 2. Behavior of DYNA material models in uniaxial compression test. a) Stress vs. strain behavior b) Lateral vs. axial displacement of the unit cube element used.

Typical spaceframe applications call for light-weight members, so foam filling must be shown to be weight-effective for a given application. We conducted preliminary numerical studies on foam-filled and unfilled, steel hat sections in order to discover ways of improving both structural performance of the sections (e.g. strength and energy absorption on a per unit weight basis) and the numerical modeling technology. The goal of these studies was to develop reliable finite element predictions of the response of spaceframes subjected to severe impact loads. In addition to the hat section and chassis examples below, we have previously used DYNA material models 5, 26, and 35 to study the axial buckling crush of foam-filled aluminum extrusions (Logan, 1995).

3.1 Sheet steel hat section in bending

Data furnished in 3M product information compared the energy absorption of unfilled and filled, steel hat section, box beams in four-point bend tests. Simulations of these tests were performed using available data for both unfilled and filled

conditions, as shown in the DYNA3D output in Fig. 3. Load vs. deflection behavior is shown in Fig. 4. For the unfilled box, the steel thickness and yield were adjusted to approximately match the test data, as these values were not available in the product brochure or on consulting 3M. After obtaining a good match to the unfilled data, Model 335 and parameters chosen as a best fit to data supplied on a 3M Brand Syntactic Foam made from Scotchlite™ glass microbubble technology were used. The first run with DYNA3D closely approximated the reported data for the filled condition, indicating specific energy absorption in the range of 56 kJ/kg for the simple bend test.

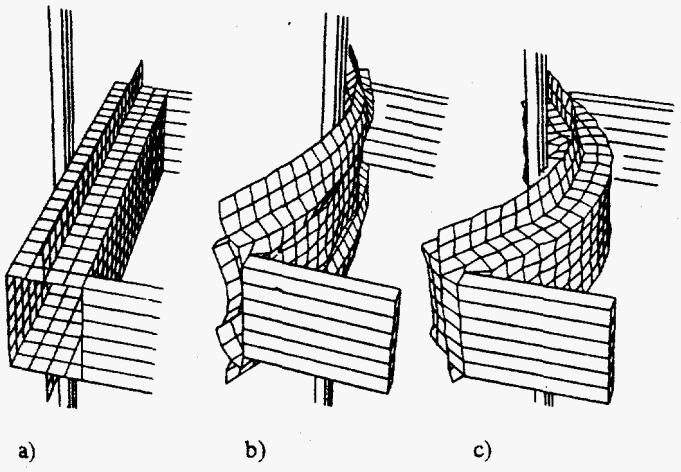

FIGURE 3: DYNA3D analysis of foam fill on hat section box beam in bending ; a) undeformed, b) deformed, no fill, c) deformed, foam filled. Foam increment is 56 kJ/kg.

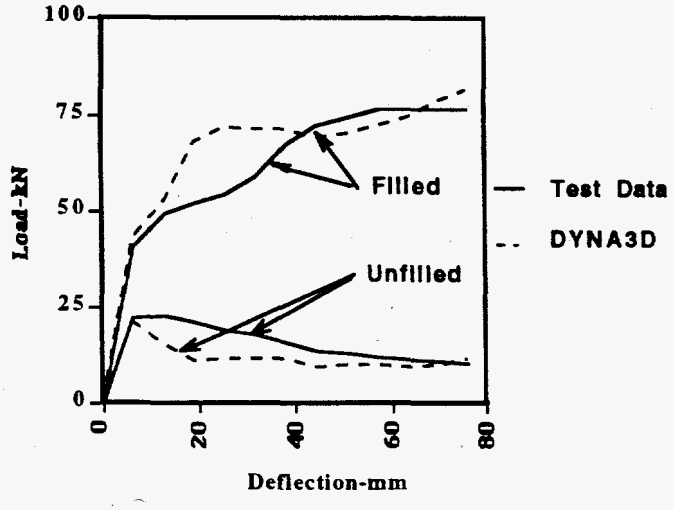

FIGURE 4: Load vs. deflection in the 4-point bend test. Solid lines are test data for unfilled and filled, hat section, box beams, dashed lines are DYNA3D results with Model 335 foam.

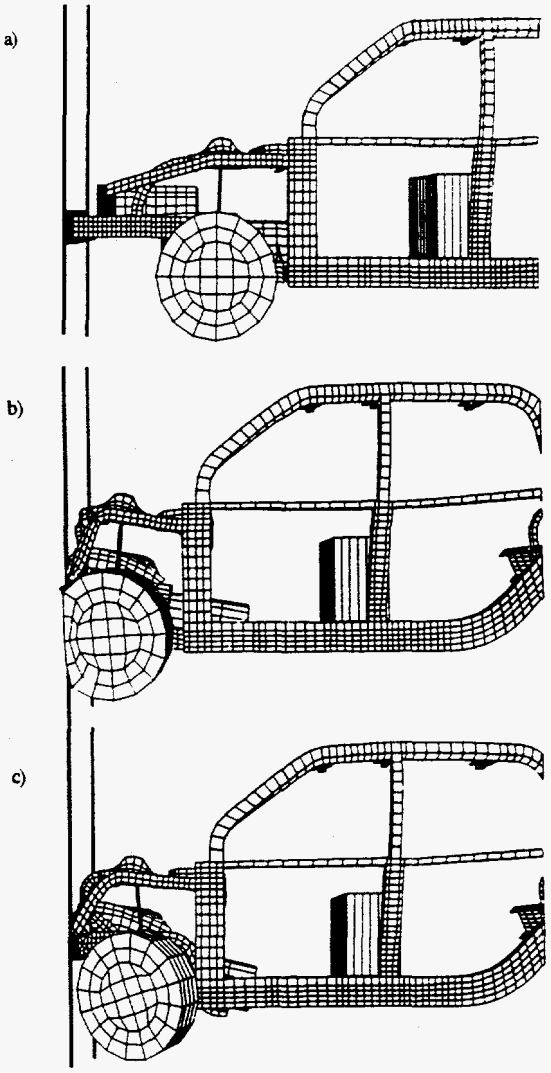

FIGURE 5: Effect of midrail foam fill on Running Chassis "M" design; a) undeformed, b) 50 cm crush, no foam fill, c) 50 cm crush, foam filled midrail. Foam increment is 16 kJ/kg.

3.2 Application to an Aluminum Spaceframe Chassis

With a relatively quick success at capturing the energy absorption effect of the foam fill, we chose as an example of a real-world application the midrail for the Running Chassis "M" design (Logan et al., 1995) in a frontal impact test. The undeformed chassis is shown in Fig. 5a, with the deformed configuration at 50 cm of crush shown in Fig. 5b for the unfilled midrail. In Fig. 5c, the chassis is shown at the same 50 cm crush point with the midrail filled with 3M Macrolite™ composite foam, a product similar in behavior but somewhat weaker and less dense than the prior Syntactic Foam. Buckling of the midrail is inhibited in both the axial and bending modes in the 'S' portion forward of the A-Pillar. As a result, the midrail tends to rotate more in a rigid fashion, forcing additional deformation of the

surrounding chassis members. One obvious result of this, as shown, is enhanced rotation of the wheel/tire assembly. Since the dynamic loads can be redistributed among the structural members during the frontal crush, as opposed to the simple bend test above, the high energy absorption value of 56 kJ/kg is not achieved. Rather, approximately 16 kJ/kg is observed as the contribution due to foam fill of the midrail. This value is certainly respectable as an addition to the optimized "M" design, but is not far above the slope of the extrusions themselves as observed in the design paper (Logan et al., 1995).

4. APPLICATIONS - AT-400A SHIPPING CONTAINER

As part of our continuing evaluation of the design of the AT-400A shipping container, we constructed a model of the overpack and containment vessel (refer to Figure 6). The overpack consists of a cylindrical stainless steel drum and cylindrical liner separated by foamed-in-place, rigid, polyurethane foam, and two removable inserts. The inserts consist of a thin aluminum skin surrounding foamed-in-place, rigid, polyurethane foam. The containment vessel is a circumferentially welded, stainless steel, pressure vessel consisting of a cylindrical midsection and semi-elliptical heads. This container was subjected to two accident environments selected from regulatory sources governing the transportation of Type B shipping containers. The two environments were: 1) from 10CFR71, dropping the container from a height of 9 m onto a rigid surface (rigid wall boundary in DYNA3D), and 2) from IAEA Safety Series 6, dropping a 1 m^2, 500 kg, mild steel plate from 9 m onto the container. There were two objectives in modeling these environments. The first objective was to examine the effect of foam modeling methodology on overpack deformation using the data decks for Models 5, 10, 26, and 335 developed for the uniaxial test in Fig. 2. The second objective was to demonstrate the severity of the IAEA dynamic crush environment relative to the 10CFR71 drop environment. Among the proposed changes to 10CFR71 which were published in the Federal Register in June of 1988 was the incorporation of the dynamic crush environment from IAEA into the Hypothetical Accident Conditions. A relative comparison of the deformations induced in the container by the two accident environments is shown in Fig. 7.

For a 9 m side drop of the container, we observed that for this relatively isotropic foam, with minimal rate dependence, the overpack deformation was about 0.5 cm regardless of the foam model chosen. This is a result of the general uniaxial loading condition on the impacting side of the container. Stress profiles at the time of peak acceleration (about 1 ms) indicate that the stress in the direction of fall is remarkably similar for all the Models. However, the stress perpendicular to the direction of fall is quite different. It is likely that lateral expansions exhibited by Models 5 and 10 have produced an artificially high state of confinement, while Models 26 and 335 indicate very little overall confinement. Since the integrity of the container lid, for example, depends in part on the overall compressive state in the container, we feel it is important to use a model such as 26 or 335 for this type of material to provide accurate behavior in both the direction of load and in the direction perpendicular to loading.

The dynamic crush environment, applied to the side of the container, produced a peak deformation of the overpack, in the direction of loading, ranging from 2.6 cm to 2.8 cm depending upon the Model chosen. Therefore, for this container, the dynamic crush induced deformations which were more than five times greater than the deformations due to the 9 m drop of the container. Though the ratio of the deformations will vary depending upon the mass and design of a particular container, this example indicates that Type B packages certified under the current 10CFR71 regulations may not be capable of being recertified in the future if the dynamic crush environment is incorporated into the Hypothetical Accident Conditions. Another tendency we observed was a wide variation in the amount of foam deformation which was elastically recovered after application of the dynamic crush. The permanent deformation of the foam, in the direction of loading, varied from 2.0 cm to 2.7 cm for the Models. This variation in unloading behavior could significantly affect attempts to validate numerical results with test results, since deformation measurements are typically of the final deformed shape of the container.

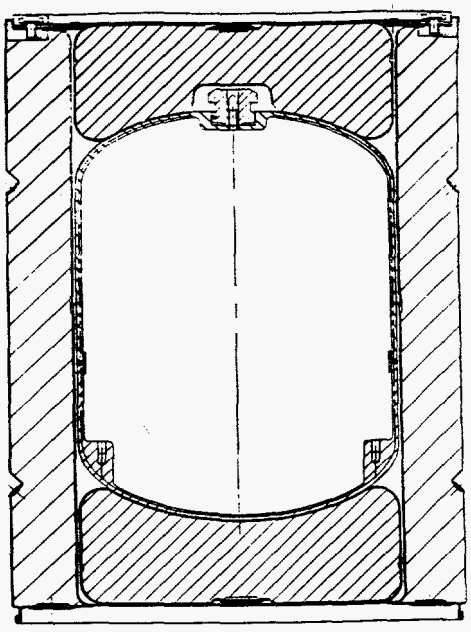

FIGURE 6. The AT-400A is a drum-type container which is being designed to endure both a 9 m drop and the impact of a 500 kg plate dropped from 9 m onto the container.

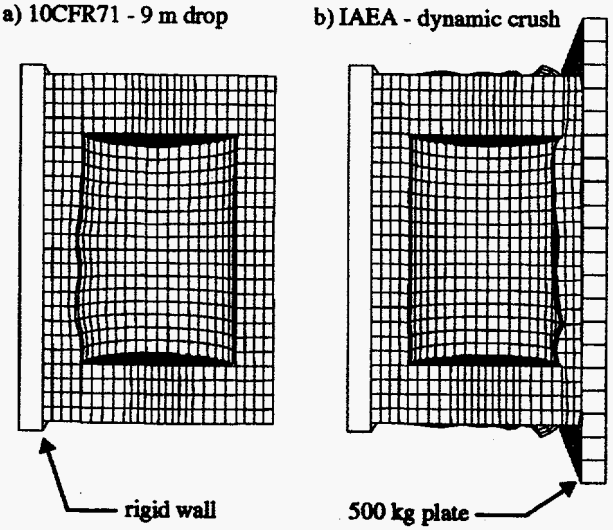

Displacements have been scaled by a factor of 3 in both plots.

FIGURE 7. Deformations induced in the AT-400A overpack by the dynamic crush environment were far more severe than those induced by the 9 m drop. Incorporation of the IAEA dynamic crush environment into 10CFR71, as proposed in June of 1988, could therefore prevent some current Type B shipping container designs from being recertified.

5. CONCLUSIONS AND FUTURE WORK

We have demonstrated, with versions of LLNL's DYNA code, the importance of foam fill for energy absorption and thus impact mitigation. The effect of foam fill was shown in terms of specific energy absorption in a steel hat section and in an aluminum spaceframe design. To show this effect, we used a new crushable material model developed for anisotropy of elasticity, crush, and deviatoric plasticity. In addition, this model (335) is invariant in the isotropic case, and offers strain and rate dependence of plastic flow. The ability of this model to simulate foam crush was compared to other models available in the current version of DYNA3D. Our conclusion, based on simulations of a single element and of the AT-400A shipping container, is that for rate-independent cases, Model 26 is the most appropriate pre-existing material model. This model must be used with caution due to its non-invariant nature in the isotropic case. Still, we feel that (possible) errors in the stress level of the foam on the order of 1.15 are of less consequence than the unpredictable presence of artificial lateral expansions which may be encountered with Models 5, 10, or 16. We anticipate further developments to Model 335 as it is used to model applications which make use of its rate dependence, anisotropy of crush and plastic flow, and tensile behavior. Such applications might include modeling low density open-cell foams and the design of spaceframe extrusion structures. The development of advanced material models, such as Model 335, has a dual benefit in allowing more effective mitigation of impact in weapon shipping containers as well as enhanced chassis designs for future vehicles.

ACKNOWLEDGMENTS

The authors acknowledge the continued support of G.L. Dittman and R.E. Clough in bringing this work to fruition. Helpful discussions were had with T.E. Healy and M. Puso of LLNL on foam properties, and with R.D. Parkinson of Kaiser Aluminum on foam crush and data for the box beam and extrusion cases. This work was performed under the auspices of the U.S. Department of Energy by the Lawrence Livermore National Laboratory under contract W-7405-Eng-48.

REFERENCES

Drucker, D.C. and Prager, W. (1952). "Soil Mechanics and Plastic Analysis of Limit Design", *Quart. Appl. Math. 10*, No. 2, pp. 157-165.

Gibson, L.J., and Ashby, M.F. (1988). *Cellular Solids: Structure and Properties*. Pergamon Press, Elmsford, N.Y.

Gibson, L.J., Ashby, M.F., Zhang, J., and Triantafillou, T.C. (1989). "Failure Surfaces for Cellular Materials Under Multiaxial Loads - I. Modeling", *Int. J. Mech. Sci. 31*, No. 9, pp. 635-663

Green, S.J., Schierloh, R.D., Perkins, R.D., and Babcock, S.G. (1969). "High-velocity Deformation Properties of Polyurethane Foams," *Exp. Mech.*, Vol. 9, No. 3, pp. 103-109.

Hill, R. (1948). *The Mathematical Theory of Plasticity*, Clarendon Press, Oxford.

Key, S.W. (1974). "HONDO - A Finite Element Computer Program for the Large Deformation Dynamic Response of Axisymmetric Solids," Sandia National Laboratories, Albuquerque, NM, Report 74-0039.

Krieg, R.D. (1972). "A Simple Constitutive Description for Cellular Concrete", Sandia National Laboratories, Albuquerque, NM, Report SC-DR-72-0883.

Logan, R.W. (1995). "AMMP: Advanced Material Models Project," *Engineering Research and Development Thrust Area Report FY94*, ed. G.L. Goudreau, LLNL, UCRL-53868-94.

Logan, R.W., Perfect, S.A., and Parkinson, R.D. (1995). "Energy Absorption in Aluminum Extrusions for a Spaceframe Chassis", *Proc. IX Intl. Conf. on Vehicle Structural Mechanics*, Troy, MI Apr. 4-5, SAE .

Maiti, S.K., Gibson, L.J., and Ashby, M.F. (1984). "Deformation and Energy Absorption Diagrams for Cellular Solids," *Acta Metallurgica*, Vol. 32, No. 11, pp. 1963-1975.

Whirley, R.G., and Hallquist, J.O. (1991). "DYNA3D: A Nonlinear, Explicit, Three-Dimensional Finite Element Code for Solid and Structural Mechanics- User Manual," University of California, Lawrence Livermore National Laboratory, Report UCRL-MA-107254.